Time-dependent Aero-acoustic Adjoint-based Shape Optimization of Helicopter Rotors in Forward Flight

Enrico Fabiano * Asitav Mishra † Dimitri Mavriplis ‡

Department of Mechanical Engineering, University of Wyoming, Laramie, WY 82071-3295.

Karthik Mani §

Rolls-Royce Corporation, Indianapolis, IN 46225.

A formulation for the sensitivity analysis of time-dependent helicopter rotor aeroacoustic problems is presented in this paper. The hybrid aeroacoustic approach, in which a near body CFD solver is coupled to an FW-H acoustic module that propagates the rotor noise signature to a far field observer, has been followed in this work. Both forward and adjoint sensitivity formulations are derived that correspond to analogues of the aeroacoustic analysis problem. The fully coupled aeroacoustic analysis formulation is first verified to effectively perform noise predictions of a four bladed HART2 rotor in trimmed forward flight. Upon successful verification, the adjoint formulation is used to minimize helicopter rotor noise signatures via blade shape optimization.

I. Introduction

Adjoint equations, which have been used extensively for aerodynamic shape optimization problems using computational fluid dynamics (CFD),[1–9] are a very powerful tool in the sense that they allow the computation of sensitivity derivatives of an objective functional to a set of given inputs at a cost which is essentially independent of the number of inputs. Adjoint-based shape optimization for steady-state problems is now fairly well established in the aircraft industry for both two-dimensional and three-dimensional problems.[5,10] However, the development of adjoint methods for gradient-based shape optimization of unsteady flow problems has been hindered by the inherent computational cost and the complexity of the associated flow physics. Feasibility of the unsteady adjoint approach in three-dimensional problems was done by Mavriplis[10] while full implementation in a general sense and application to large scale problems involving helicopter rotors was then carried out by Nielsen et. al. in the NASA FUN3D code.[11] Extension of the adjoint method to multidisciplinary design optimization problems has mainly focused on fluid-structure interaction applications in the context of both fixed and rotary wing aircraft.[12,13] Here we extend the three dimensional multidisciplinary adjoint method to the problem of rotorcraft noise mitigation. Because of the ever more stringent requirement on rotorcraft noise, rotor aeroacoustics takes on a leading role in the helicopter design process. Typically rotor noise has been addressed by judicious selection of rotor blade configurations, airfoils, planform and tip shapes.[14] Active control techniques have also been investigated.[14,15] While these methods mainly rely on expensive wind tunnel experiments and on the experience of the aircraft designer, few attempts have been made at exploiting shape optimization techniques in the context of noise reduction, focusing mainly on two dimensional[16,17] or sonic boom applications.[6,18] In previous work[19] we have derived the coupled adjoint aeroacoustic problem for a two dimensional airfoil representative of a blade vortex interaction problem and demonstrated the feasibility of the unsteady aeroacoustic optimization. Here we develop a three dimensional unsteady adjoint methodology that allows the use of gradient based optimization methods for rotor aeroacoustic applications, so that passive noise minimization techniques can be exploited without incurring significant performance penalties through the application of optimal shape modifications.

The paper is structured as follows: section II describes the aerodynamic flow solver, section III details the aerodynamic sensitivity analysis formulation, section IV introduces the FW-H integration module and its sensitivity formulation. In

*PhD candidate; efabiano@uwyo.edu

†Post doctoral researcher; amishsra3@uwyo.edu

‡Professor; mavripl@uwyo.edu

§CFD specialist Rolls-Royce Corporation; karthik.mani@rolls-royce.com

section V we show aeroacoustic optimization results while in section VI we draw conclusions from the current work and highlight future applications.

II. Aerodynamic Analysis and Sensitivity Formulation

II.A. Flow Solver Analysis Formulation

The base flow solver used in this work is the NSU3D unstructured mesh Reynolds-averaged Navier-Stokes solver. NSU3D has been widely validated for steady-state and time-dependent flows and contains a discrete tangent and adjoint sensitivity capability which has been demonstrated previously for optimization of steady-state and time-dependent flow problems. As such, only a concise description of these formulations will be given in this paper, with additional details available in previous references.[10,20–22] The flow solver is based on the conservative form of the Navier-Stokes equations which may be written as:

$$\frac{\partial \mathbf{U}(\mathbf{x},t)}{\partial t} + \nabla \cdot \mathbf{F}(\mathbf{U}) = 0 \tag{1}$$

For moving mesh problems these are written in arbitrary Lagrangian-Eulerian (ALE) form as:

$$\frac{\partial V\mathbf{U}}{\partial t} + \int_{dB(t)} [\mathbf{F}(\mathbf{U}) - \dot{\mathbf{x}}\mathbf{U}] \cdot \mathbf{n} dB = 0 \tag{2}$$

Here V refers to the area of the control volume, $\dot{\mathbf{x}}$ is the vector of mesh face or edge velocities, and $\mathbf{n}$ is the unit normal of the face or edge. The state vector $\mathbf{U}$ consists of the conserved variables and the Cartesian flux vector $\mathbf{F} = (\mathbf{F}_x, \mathbf{F}_y, \mathbf{F}_z)$ contains both inviscid and viscous fluxes. The equations are closed with the perfect gas equation of state and the Spalart-Allmaras turbulent eddy viscosity model[23] for all cases presented in this work.

The solver uses a vertex-centered median dual control volume formulation that is second-order accurate, where the inviscid flux integral S around a closed control volume is discretized as:

$$S = \int_{dB(t)} [\mathbf{F}(\mathbf{U}) - \dot{\mathbf{x}}\mathbf{U}] \cdot \mathbf{n} dB = \sum_{i=1}^{n_{edge}} \mathbf{F}_{e_i}^{\perp}(V_{e_i}, \mathbf{U}, \mathbf{n}_{ei}) B_{e_i} \tag{3}$$

where B_e is the face area, V_e is the normal face velocity, $\mathbf{n}_e$ is the unit normal of the face, and $F_e^{\perp}$ is the normal flux across the face. The time derivative term is discretized using a second-order accurate backward-difference formula (BDF2) scheme. Denoting the spatially discretized terms at time level n by the operator $S^n(\mathbf{U}^n)$, the resulting system of non-linear equations to be solved for the analysis problem at each time step can be written as:

$$\mathbf{R}^n = \frac{\frac{3}{2}V^n\mathbf{U}^n - 2V^{n-1}\mathbf{U}^{n-1} - \frac{1}{2}V^{n-2}\mathbf{U}^{n-2}}{\Delta t} + S^n(\mathbf{U}^n) = 0 \tag{4}$$

which in simplified form exhibiting the functional dependencies on $\mathbf{U}$ and $\mathbf{x}$ at different time levels is given as:

$$\mathbf{R}^n(\mathbf{U}^n, \mathbf{U}^{n-1}, \mathbf{U}^{n-2}, \mathbf{x}^n, \mathbf{x}^{n-1}, \mathbf{x}^{n-2}) = 0 \tag{5}$$

At each time step n, the implicit residual is linearized with respect to the unknown solution vector $\mathbf{U}^n$ and solved for using Newton's method as:

$$\begin{gathered} \left[\frac{\partial \mathbf{R}^k}{\partial \mathbf{U}^k}\right] \delta\mathbf{U}^k = -\mathbf{R}^k \\ \mathbf{U}^{k+1} = \mathbf{U}^k + \delta\mathbf{U}^k \\ \delta\mathbf{U}^k \rightarrow 0, \mathbf{U}^n = \mathbf{U}^k \end{gathered} \tag{6}$$

The Jacobian matrix is inverted iteratively using a line-implicit agglomeration multigrid scheme that is applied as a preconditioner for a GMRES Krylov solver.[24]

Although the above equation denotes the solution at a single time level n, for the remainder of this paper we will use the generalized notation:

$$\mathbf{R}(\mathbf{U}, \mathbf{x}) = 0 \tag{7}$$

where the vector $\mathbf{U}$ denotes the flow values at all time steps, and where each (block) row in this equation corresponds to the solution at a particular time step as given in equation (5). Equation (7) denotes the simultaneous solution of all time steps and is solved in practice by Newton's method using forward block substitution (i.e. forward integration in time) since each new time step depends on the previous two time levels.

II.B. Mesh deformation capability

In order to deform the mesh for time-dependent problems a linear elastic analogy mesh deformation approach has been implemented. In this approach, the mesh is modeled as a linear elastic solid with a variable modulus of elasticity that can be prescribed either as inversely proportional to cell volume or to the distance of each cell from the nearest wall.[25,26] The resulting equations are discretized and solved on the mesh in its original undeformed configuration in response to surface displacements using a line-implicit multigrid algorithm analogous to that used for the flow equations. The governing equations for mesh deformation can be written symbolically as:

$$\mathbf{G}(\mathbf{x}, \mathbf{x_{surf}}(\mathbf{D})) = \mathbf{0} \tag{8}$$

where $\mathbf{x}$ denotes the interior mesh coordinates and $\mathbf{x_{surf}}(\mathbf{D})$ are the surface mesh coordinates that depend on the pitch design variables, described in section III.A, and the shape parameters that define the surface geometry.

III. Aerodynamic Sensitivity Analysis Formulation

The basic sensitivity analysis implementation follows the strategy developed in references.[10,20] Consider an arbitrary objective function L that is evaluated using the unsteady flow solution set $\mathbf{U}$ and unsteady mesh solution set $\mathbf{x}$ expressed as:

$$L = L(\mathbf{U}, \mathbf{x}) \tag{9}$$

Assuming that the state variables (i.e.$\mathbf{U}, \mathbf{x}$) are dependent on some input design parameters $\mathbf{D}$, the total sensitivity of the objective function L to the set of design inputs can be expressed as the inner product between the vector of state sensitivities to design inputs and the vector of objective sensitivities to the state variables as:

$$\frac{dL}{d\mathbf{D}} = \begin{bmatrix} \frac{\partial L}{\partial \mathbf{x}} & \frac{\partial L}{\partial \mathbf{U}} \end{bmatrix} \begin{bmatrix} \frac{\partial \mathbf{x}}{\partial \mathbf{D}} \\ \frac{\partial \mathbf{U}}{\partial \mathbf{D}} \end{bmatrix} \tag{10}$$

The non-linear flow residual operator and the linear elasticity mesh residual operator as described earlier provide the constraints which can be expressed in general form over the whole space and time domains as:

$$\begin{aligned} \mathbf{G}(\mathbf{x}, \mathbf{D}) &= 0 \\ \mathbf{R}(\mathbf{U}, \mathbf{x}) &= 0 \end{aligned} \tag{11}$$

which when linearized with respect to the design inputs yields:

$$\begin{bmatrix} \frac{\partial \mathbf{G}}{\partial \mathbf{x}} & 0 \\ \frac{\partial \mathbf{R}}{\partial \mathbf{x}} & \frac{\partial \mathbf{R}}{\partial \mathbf{U}} \end{bmatrix} \begin{bmatrix} \frac{\partial \mathbf{x}}{\partial \mathbf{D}} \\ \frac{\partial \mathbf{U}}{\partial \mathbf{D}} \end{bmatrix} = \begin{bmatrix} -\frac{\partial \mathbf{G}}{\partial \mathbf{D}} \\ 0 \end{bmatrix} \tag{12}$$

These constitute the forward sensitivity or tangent sensitivity equations. The mesh and flow sensitivity vectors can then be substituted into equation (10) to obtain the complete sensitivity of the objective with respect to the design variable $\mathbf{D}$.

The forward sensitivity approach requires a new solution of equation (12) for each design parameter $\mathbf{D}$. On the other hand, the adjoint approach can obtain the sensitivities for any number of design inputs $\mathbf{D}$ at a cost which is approximately independent of the number of design variables. The adjoint problem can be obtained by pre-multiplying equation (12) by the inverse of the large coupled matrix and substituting the resulting expression for the sensitivities into equation (10) and defining adjoint variables as the solution of the system:

$$\begin{bmatrix} \frac{\partial \mathbf{G}}{\partial \mathbf{x}}^T & \frac{\partial \mathbf{R}}{\partial \mathbf{x}}^T \\ 0 & \frac{\partial \mathbf{R}}{\partial \mathbf{U}}^T \end{bmatrix} \begin{bmatrix} \Lambda_{\mathbf{x}} \\ \Lambda_{\mathbf{U}} \end{bmatrix} = \begin{bmatrix} \frac{\partial L}{\partial \mathbf{x}}^T \\ \frac{\partial L}{\partial \mathbf{U}}^T \end{bmatrix} \tag{13}$$

where $\Lambda_{\mathbf{U}}$ and $\Lambda_{\mathbf{x}}$ are the flow and mesh adjoint variables respectively. The final objective sensitivities can be obtained as:

$$\frac{dL}{d\mathbf{D}}^T = \begin{bmatrix} \frac{\partial \mathbf{G}}{\partial \mathbf{D}}^T & 0 \end{bmatrix} \begin{bmatrix} \Lambda_{\mathbf{x}} \\ \Lambda_{\mathbf{u}} \end{bmatrix} \tag{14}$$

Recalling that equations (12) and (13) apply over the entire time domain, equation (12) represents a forward time integration while the back-substitution procedure in equation (13) leads to a reverse integration in time, beginning with the last physical time step and proceeding to the initial time step. A more detailed description of the complete formulation is presented in,[27,28] where the procedure has been used to perform aerodynamic shape optimization for a rigid rotor.

III.A. Rotor pitch formulation for forward flight

Since the goal of this work is to optimize a rotor in trimmed forward flight, the rotor blade pitch angle must be included as a control input so that the rotor can attain the required thrust and lateral moments. The pitch angle can be represented as a combination of a mean pitch angle and several harmonic components:

$$\theta = \theta_0 + \sum_{i=1}^{n} \theta_{c_i} \cos(i\psi) + \sum_{i=1}^{n} \theta_{s_i} \sin(i\psi) \tag{15}$$

where ψ is the rotor azimuth. In this work we use only one harmonic, hence $i = 1$, and the design variables $\mathbf{D_{pitch}} = [\theta_0, \theta_{1c}, \theta_{1s}]$ are to be chosen such that the rotor is trimmed, where $\boldsymbol{\theta_0}$ is the collective and $\boldsymbol{\theta_{1c}}, \boldsymbol{\theta_{1s}}$ the two cyclics pitch parameters. To incorporate rotor pitch actuation in the CFD analysis a blade surface pitch actuation equation (in residual form)

$$\mathbf{S}^{\theta} = \mathbf{x}_{\mathbf{s}\theta} + \left[\mathbf{T}^{\theta}\left(\theta(\mathbf{D})\right)\right]\mathbf{x} = \mathbf{0} \tag{16}$$

and a mesh motion equation

$$\mathbf{G}^{'}\left(\mathbf{x}_{\theta}, \mathbf{x}_{\mathbf{s}\theta}\right) = \mathbf{0} \tag{17}$$

must be taken into account. Finally, after introducing an equation for the mesh azimuthal rotation in residual form

$$\mathbf{S}^{\Psi} = \mathbf{x}_{\mathbf{p}} + \left[\mathbf{T}^{\Psi}\right]\mathbf{x}_{\theta} = \mathbf{0} \tag{18}$$

the analysis problem can be formulated as

$$\begin{aligned} \mathbf{G}(\mathbf{x}, \mathbf{D}) &= \mathbf{0} \\ \mathbf{S}^{\theta}(\mathbf{x}_{\mathbf{s}\theta}, \mathbf{x}, \mathbf{D}) &= \mathbf{0} \\ \mathbf{G}^{'}(\mathbf{x}_{\theta}, \mathbf{x}_{\mathbf{s}\theta}) &= \mathbf{0} \\ \mathbf{S}^{\Psi}(\mathbf{x}_{\mathbf{p}}, \mathbf{x}_{\theta}) &= \mathbf{0} \\ \mathbf{R}(\mathbf{U}, \mathbf{x}_{\mathbf{p}}) &= \mathbf{0} \end{aligned} \tag{19}$$

where $\left[\mathbf{T}^{\theta}\right]$ and $\left[\mathbf{T}^{\Psi}\right]$ are matrix representation for the pitch actuation and the azimuthal rotation respectively, $\mathbf{x}_{\mathbf{s}\theta}$ denotes the blade surface mesh coordinates after pitch, $\mathbf{x}_{\theta}$ the interior mesh coordinates after mesh motion due to pitch and $\mathbf{x}_{\mathbf{p}}$ the surface and interior mesh coordinates after pitch and azimuthal rotation, while $\mathbf{U}$ is the unsteady flow solution. The forward and adjoint sensitivity formulation can now be derived, as described in the previous section, by differentiating and transposing the system of coupled equations (19) instead of equations (11), as detailed by Mishra.[29]

IV. Aeroacoustic model: Analysis and Sensitivity Formulation

Despite the continuous increase in computational resources, numerical simulations that resolve wave propagation from the nearfield to a farfield observer are still infeasible, hence a viable approach to predicting farfield noise level is the use of hybrid methods that have been developed over the years[30] and are now fairly well established.
In hybrid methods the finely resolved nearfield flow time history is used as input to an acoustic formulation that predicts the noise radiated to a given observer. The acoustic formulations are often based on Lighthill's acoustic analogy, in

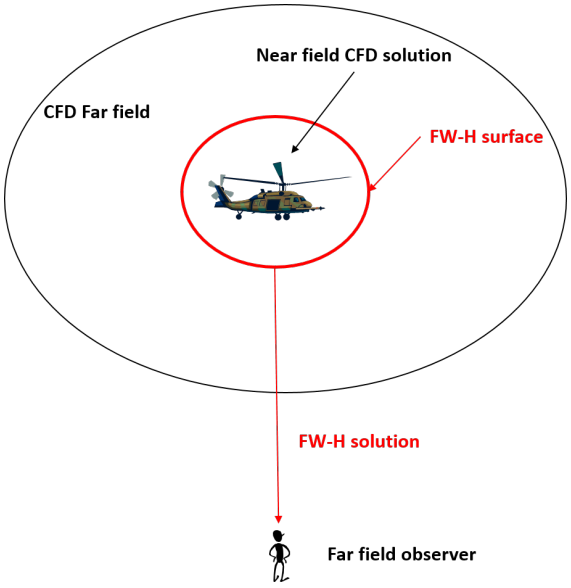

(a) Schematic of the hybrid approach for the aeroacoustic computation

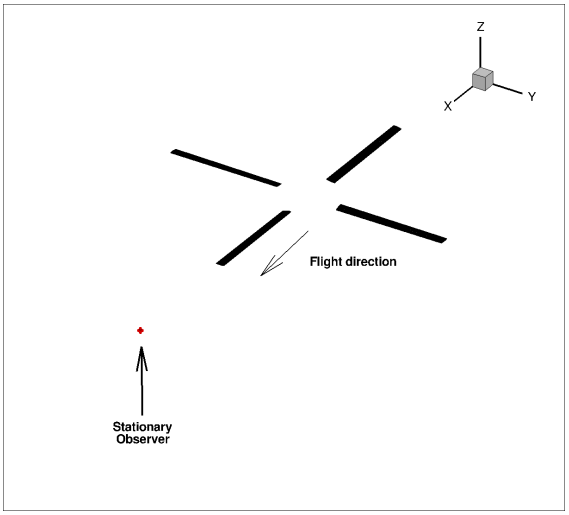

(b) Acoustic integration surface and observer location

Figure 1. Schematics of the hybrid acoustic approach (a) and acoustic problem formulation (b): the observer is stationary in the plane of the rotor one radius ahead of the rotor disk.

particular the Ffowcs Williams-Hawkings (FW-H) approach, which is the one used in this work.[31]
Here the NSU3D CFD flow solver provides the nearfield flow time history to a newly developed FW-H acoustic integration module that propagates the acoustic pressure at a farfield observer. A schematic of the hybrid approach is shown in Figure 1(a). The location of the FW-H acoustic integration surface depends on the noise problem being investigated. When significant non-linear flow effects are present, as in the case of high speed helicopter forward flight, an off-body permeable integration surface should be used.[30,32] Noise prediction with an off-body permeable surface is only accurate when the flow field between the body and the integration surface is finely resolved, resulting in a significant increase in the computational cost of the CFD time integration process. However, the case considered in this work consists of a Hart2[33] four-bladed rotor in forward flight with a freestream mach number 0.095 and a tip Mach number of 0.638. At these conditions nonlinear flow effects are expected to be negligible so that an on-body impermeable integration surface can be used. Figure 1(b) shows the FW-H acoustic integration surface and the observer location used for validation purposes. The acoustic surface coincides with the CFD rotor surface mesh and every node on the surface is an acoustic source that produces an acoustic pressure at the observer location via the FW-H integration process. Coupling the linearization of the acoustic module to the linearization of the flow solver allows for the computation of the adjoint sensitivity of the acoustic objective function with respect to the full vector of design variables to be used in the gradient-based shape optimization process.

IV.A. Acoustic Analysis Formulation: the FW-H equation

The FW-H equation can be expressed in differential form as[30]

$$\left(\frac{\partial^2}{\partial t} - c_0^2 \frac{\partial^2}{\partial x_i \partial x_j}\right)\left(H(f)\rho'\right) = -\frac{\partial F_i \delta(f)}{\partial x_i} + \frac{\partial Q \delta(f)}{\partial t} \tag{20}$$

where

$$Q_i = \left(\rho_o v_i + \rho\left(u_i - v_i\right)\right)\frac{\partial f}{\partial x_i} \tag{21}$$

and

$$F_i = \left(p\delta_{ij} + \rho u_i\left(u_j - v_j\right)\right)\frac{\partial f}{\partial x_i} \tag{22}$$

and the Lighthill's stress tensor, the quadrupole term, has been omitted since it is not used in this work. Equation (21) gives rise to an unsteady monopole-type contribution that can be associated with mass addition, while the dipole term, equation (22), involves an unsteady force. The function $f(x_i,t)=0$ defines the surface of integration outside of which the solution is sought. Total density and pressure are ρ and p respectively, the fluid velocities are u_i, while v_i are the surface velocities and c_o is the freestream speed of sound. The prime denotes perturbation relative to the freestream which itself is denoted with the subscript o. x_i and t are Cartesian coordinates and time respectively. $H(f)$ is the Heaviside function while $\delta(f)$ is the Dirac function. A time domain solution to equation (20) can be obtained from the derivation of Farassat[34] using the variables

$$\begin{aligned} U_i &= \left(1-\frac{\rho}{\rho_o}\right)v_i+\frac{\rho u_i}{\rho_o} \\ L_i &= p' n_j + \rho u_i (u_n - v_n) \end{aligned} \tag{23}$$

as proposed by Di Francescantonio,[35] where $p'=p-p_o$, $u_n=u_i n_i$, $v_n=v_i n_i$ and n_i is the unit normal of the acoustic surface. The integral solution is then given, neglecting the quadrupole term, by equation (24)

$$\begin{aligned} 4\pi p'_T(\mathbf{y},t) &= \int_{f=0}\left[\frac{\rho_o\left(\dot{U}_n+U_{\dot{n}}\right)}{r(1-M_r)^2}\right]_{ret}dS+\int_{f=0}\left[\frac{\rho_o U_n K}{r^2(1-M_r)^3}\right]_{ret}dS \\ 4\pi p'_L &= \frac{1}{c_o}\int_{f=0}\left[\frac{\dot{L}_r}{r(1-M_r)^2}\right]_{ret}dS+\int_{f=0}\left[\frac{L_r-L_M}{r^2(1-M_r)^2}\right]_{ret}dS+\frac{1}{c_o}\int_{f=0}\left[\frac{L_r K}{r^2(1-M_r)^3}\right]_{ret}dS \\ 4\pi p'(\mathbf{y},t) &= 4\pi p'_T(\mathbf{y},t)+4\pi p'_L(\mathbf{y},t) \end{aligned} \tag{24}$$

where $\mathbf{y}$ is the observer location, t is the observer time, r is the distance between the source $\mathbf{x}$ and the observer $\mathbf{y}$, M is the surface Mach number and

$$\begin{aligned} U_n &= U_i n_i \\ M_r &= M_i r_i \\ L_r &= L_i r_i \\ L_M &= L_i M_i \\ K &= r\dot{M}_r + c_o(M_r - M^2) \end{aligned} \tag{25}$$

Equation (24) requires the evaluation of the integrals at the emission or retarded time τ: for a given observer location $\mathbf{y}$ and time t the retarded time must be computed via the solution of the nonlinear equation (26)

$$\tau = t - r(\mathbf{x}(\tau),\mathbf{y})/c_o \tag{26}$$

where $r(\mathbf{x}(\tau),\mathbf{y})$ is the distance between the source $\mathbf{x}$ at the emission time τ and the observer $\mathbf{y}$. This approach has been followed in most acoustic-analogy-based codes.[30] However, by regarding the source time as the primary time one can choose the source time for an acoustic source and determine when the signal will reach the observer using equation (27)

$$t = \tau + r(\mathbf{x}(\tau),\mathbf{y})/c_o \tag{27}$$

where τ is again the source time and t is the reception time, i.e. the time at which the acoustic disturbance reaches the observer. Equation (27), a rearrangmenet of equation (26), is easier to solve than its retarded time counterpart as the observer motion is usually simpler than the motion of the acoustic integration surface. For each acoustic source a sequence of uniformly spaced source times leads to a sequence of unequally spaced observer times as each source has a different source-to-observer distance, hence the acoustic pressure time history for each source must be interpolated at the desired observer time to determine the final acoustic pressure at the observer location. A comparison of the two algorithms is given in.[36]

In this work we follow this so-called source-time-dominant algorithm as it allows a seamless integration of the acoustic module with the CFD solver. The source time is the CFD time and the integrals in equation (24) are evaluated at every time step during the CFD time integration process. The acoustic integration surface corresponds to the rotor's

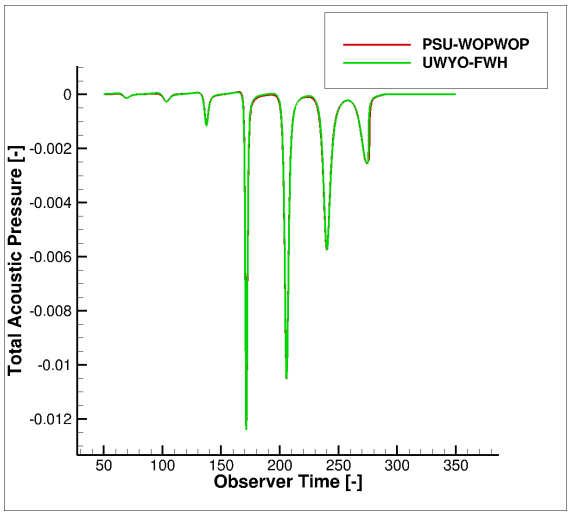

(a) Validation of the current FW-H implementation with the PSU-WOPWOP acoustic code over an extended observer time window.

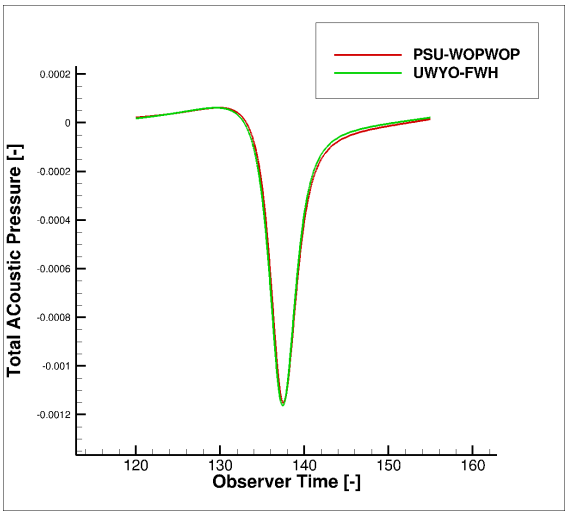

(b) Comparison between the current FW-H implementation and PSU-WOPWOP over the observer time window used for optimization purposes

Figure 2. Validation of the current FW-H implementation over an extended (a) and the optimization (b) time window

unstructured surface mesh and each node of the CFD grid corresponds to an acoustic source. All the time derivative terms in equation (24) are approximated with a BDF2 time discretization for consistency with the CFD time integration with the exception of the source acceleration term that is approximated with a second order accurate central difference scheme. The final observer pressure time history is built via linear interpolation of each source time history at the desired observer time after the CFD integration process is completed. The observer acoustic pressure time history can finally be processed to compute the aeroacoustic objective to be minimized. The aeroacoustic objective used in this work is the root mean square of the acoustic pressure time history

$$L_{FWH} = p'_{RMS} = \sqrt{\frac{\sum_{i=1}^{N_{sample}} p'^2(\mathbf{D})}{N_{sample}}} \tag{28}$$

where N_{sample} is the number of samples in the observer acoustic pressure time history and $\mathbf{D}$ is the vector of design variables. The current implementation of the FW-H integral equation has been validated against the PSU-WOPWOP[36] acoustic code for the Hart2 rigid rotor in trimmed forward flight as shown in Figure 2. The rotor has a freestream Mach number of $M = 0.095$ with a tip Mach number of $M_{tip} = 0.638$, a shaft angle $\alpha_{shaft} = 5.4\,\text{deg}$ and a Reynolds Number of 2 million. The corresponding rotor rotational speed is $\Omega = 1041\ RPM$ (advance ratio $\mu = 0.15$). The CFD simulation has been carried out for two rotor revolutions on a mesh consisting of approximately 2.32 millions nodes with a 2-degree timestep and a stationary in-plane observer located one radius ahead of the rotor as shown in Figure 1(b) and described in Table 1. Two different observer time windows are shown in Figure 2: an extended time window, Figure 2(a), and the observer time window targeted during the optimization, Figure 2(b). In both cases agreement between the new FW-H implementation and the legacy PSU-WOPWOP[36] code is excellent.

Table 1. Observer location for the acoustic objective function with respect to the rotor axis, *R* being the rotor radius

x	y	z
2R	0	0

IV.B. Sensitivity formulation for the integral FW-H equation

Computing the sensitivities of the coupled aeroacoustic problem requires the linearization of the acoustic module with respect to a design variable. The sensitivity formulation for the current implementation of the integral FW-H equation

closely mimics the linearization of the CFD code as detailed in references.[10,20] First the forward linearization of the acoustic code has been developed by exact hand-differentiation of the discretized integral FW-H equation. The forward linearization has then been transposed and applied in reverse order to obtain the adjoint sensitivity with respect to the full vector of design variables. The forward sensitivity has been validated against the complex differentiation[37] of the acoustic code. Finally the adjoint sensitivity has been validated by duality[20] with the tangent problem.

Tangent sensitivity formulation

The forward linearization of the acoustic objective function allows the computation of the objective function sensitivity with respect to a single design variable. We express the acoustic pressure at the observer location and time as

$$p'(\mathbf{y},t,\mathbf{D}) = \mathbf{FWH}(\mathbf{U}(\mathbf{D}),\mathbf{x}(\mathbf{D})) \tag{29}$$

where D is the vector of design variables and $FWH(\mathbf{U}(\mathbf{D}),\mathbf{x}(\mathbf{D}))$ represents all the discrete operations necessary to evaluate equation (24) numerically. In this expression $\mathbf{U}(\mathbf{D})$ and $\mathbf{x}(\mathbf{D})$ are the flow and mesh solution at every time step of the time integration process. The acoustic pressure tangent sensitivity time history can be expressed as

$$\frac{dp(\mathbf{y},t,\mathbf{D})}{dD} = \sum_n \frac{\partial \mathbf{FWH}}{\partial \mathbf{U^n_{FWH}}} \frac{\partial \mathbf{U^n_{FWH}}}{\partial D} + \frac{\partial \mathbf{FWH}}{\partial \mathbf{x^n_{FWH}}} \frac{\partial \mathbf{x^n_{FWH}}}{\partial D} \tag{30}$$

so that the tangent linearization of the acoustic objective function defined in equation (28) becomes:

$$\frac{dL_{FWH}}{dD} = \sum_n \frac{\partial L_{FWH}}{\partial U^n_{FWH}} \frac{\partial U^n_{FWH}}{\partial D} + \frac{\partial L_{FWH}}{\partial x^n_{FWH}} \frac{\partial x^n_{FWH}}{\partial D} = \frac{\partial p'_{RMS}}{\partial p'} \left[\sum_n \frac{\partial FWH}{\partial \mathbf{U^n_{FWH}}} \frac{\partial \mathbf{U^n_{FWH}}}{\partial D} + \frac{\partial FWH}{\partial x^n_{FWH}} \frac{\partial x^n_{FWH}}{\partial D} \right] = \frac{\partial p'_{RMS}}{\partial p'} \frac{\partial p'}{\partial D} \tag{31}$$

In equation (31) the terms $\frac{\partial U^n_{FWH}}{\partial D}$ and $\frac{\partial x^n_{FWH}}{\partial D}$ are the flow and mesh tangent sensitivity at every time step evaluated at the acoustic integration surface that are computed via the forward time integration described by equation (12). The terms $\frac{\partial \mathbf{FWH}}{\partial \mathbf{U^n_{FWH}}}$ and $\frac{\partial \mathbf{FWH}}{\partial \mathbf{x^n_{FWH}}}$ are the forward linearization of equation (24). The forward sensitivity acoustic problem proceeds in analogy with the acoustic analysis problem. The tangent flow solution and the tangent acoustic solution are carried out simultaneously: the tangent flow solution is used to assemble the forward sensitivities of all the terms in equation (25) which in turn are used to evaluate the forward sensitivity of the integral equation (24) at every timestep, resulting in an unequally spaced acoustic pressure sensitivity at the observer location for every acoustic source. The final observer acoustic pressure sensitivity time history is built via linearization of the time interpolation algorithm at the end of the time integration process allowing for the computation of the acoustic objective function sensitivity, equation (31), with respect to one design variable.

Adjoint sensitivity formulation

The adjoint sensitivity can be derived by transposing the tangent sensitivity formulation. Transposing equation (31) yields

$$\frac{dL_{FWH}}{dD}^T = \left[\sum_n \frac{\partial \mathbf{U^n_{FWH}}}{\partial D}^T \frac{\partial FWH}{\partial \mathbf{U^n_{FWH}}}^T + \frac{\partial x^n_{FWH}}{\partial D}^T \frac{\partial FWH}{\partial x^n_{FWH}}^T \right] \frac{\partial p'_{RMS}}{\partial p}^T = \sum_n \frac{\partial U^n}{\partial D}^T \frac{\partial L_{FWH}}{\partial U^n}^T + \frac{\partial x^n}{\partial D}^T \frac{\partial L_{FWH}}{\partial x^n}^T \tag{32}$$

The terms $\frac{\partial L_{FWH}}{\partial U^n}^T = \frac{\partial FWH}{\partial \mathbf{U^n_{FWH}}}^T \frac{\partial p'_{RMS}}{\partial p}^T$ and $\frac{\partial L_{FWH}}{\partial x^n}^T = \frac{\partial FWH}{\partial x^n_{FWH}}^T \frac{\partial p'_{RMS}}{\partial p}^T$ drive the adjoint backward time integration described in equation (13). The term $\frac{\partial p'_{RMS}}{\partial p}^T$ is the reverse linearization of the observer time interpolation process that needs to be evaluated before the adjoint time integration can start while the term $\frac{\partial FWH}{\partial \mathbf{U^n_{FWH}}}^T$ and $\frac{\partial FWH}{\partial x^n_{FWH}}^T$ correspond to the reverse linearization of the acoustic integrals in equation (24). At the end of the backward time integration process the full sensitivity vector of the acoustic objective function is recovered.

Sensitivity verification

The coupled tangent aeroacoustic sensitivity to be used by the gradient based optimization algorithm is verified with the complex step differentiation method. Any function $f(x)$ operating on a real variable x can be used to compute

both the function and its derivative $f'(x)$ if the input variable x and all the intermediate variables used in the discrete evaluation of $f(x)$ are redefined as complex variables. In this case for a complex input the function will produce a complex output. A Taylor series of the now complex function $f(x+ih)$, where h is a small step-size and i is the imaginary unit, reads

$$f(x+ih) = f(x) + ihf'(x) + O\left(h^2\right) \tag{33}$$

from which the real part is simply the function value at x, while from the imaginary part the function derivative can be easily evaluated as

$$f'(x) = \frac{Im\left[f(x+ih)\right]}{h} \tag{34}$$

Despite requiring a step size, as in the case of finite-differencing, the complex step method is insensitive to small step-sizes since no differencing is required. This allows the tangent formulation to be verified to machine precision. In this work a step-size of $h = 1e-31$ has been used.

For the verification study, two revolutions of the Hart-2 rigid rotor are simulated on a mesh consisting of approximately 107,000 nodes using a 2-degree timestep. The acoustic objective time history is recorded over only the last revolution for the same observer time window as in Figure 2(b) and the sensitivity is computed with respect to the twist of the root section. Figure 3 shows excellent agreement between the tangent aeroacoustic solver and its complex counterpart. Further verification of the acoustic objective function in equation (31) is shown in Table 2. The tangent

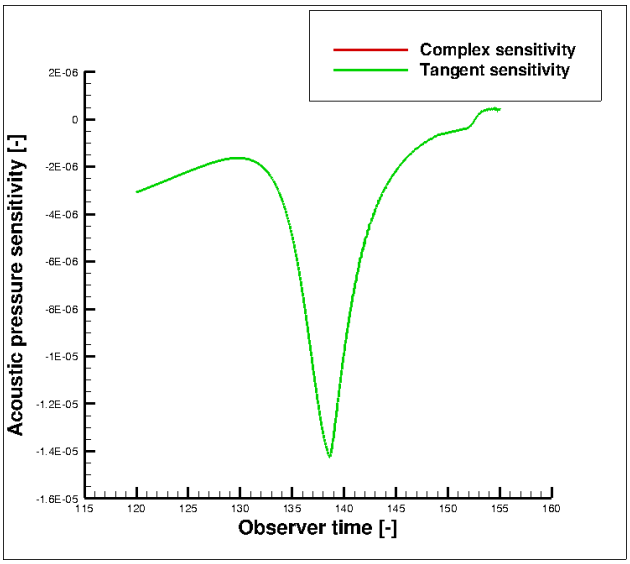

Figure 3. Complex step verification of the tangent acoustic pressure time history sensitivity

sensitivity allows for the verification of the adjoint sensitivity by the duality relation.[20] The current aeroacoustic adjoint implementation is verified in Table 2 by comparing the adjoint sensitivity to the unsteady forward and complex step sensitivities with respect to the twist of the root section. The flow equations are converged to machine precision to avoid any algebraic error, and the complex, tangent and adjoint sensitivity are seen to agree to machine precision. The adjoint sensitivity can then be used in the gradient based optimization process.

Table 2. Adjoint sensitivity verification for the p'_{RMS} objective function.

Complex	3.8549291836113**021**E-06
Tangent	3.8549291836112**867**E-06
Adjoint	3.8549291836117**472**E-06

V. Results

The goal of the present work is to reduce the noise signature of the Hart2 rotor in trimmed forward flight by means of gradient based optimization techniques that exploits the multidisciplinary aeroacoustic adjoint method developed so far. As a preliminary step the Hart2 rotor in forward flight needs to be trimmed to establish a starting point for all subsequent optimizations. The trim problem is formulated as an optimization problem described by equation (35)

$$\begin{aligned} &min\ L_{THRUST} \\ &\texttt{subject to} \\ &L_{LATERAL} = 0 \\ &w.r.t.\ \mathbf{D_{pitch}} \end{aligned} \tag{35}$$

where the vector of design variables $\mathbf{D_{pitch}}$, made up of one collective and two cyclics, is described in section III.A. One design cycle for this optimization corresponds to one unsteady flow solution and two adjoint solutions, one for the objective and one for the constrained function in equation (35).
Once the Hart2 baseline rotor has been trimmed, two different optimizations are performed. The first aeroacoustic optimization aims at reducing the rotor's noise signature under the trim constraint only, as shown in equation (36).

$$\begin{aligned} &min\ p'_{RMS} \\ &\texttt{subject to} \\ &L_{THRUST} = 0 \\ &L_{LATERAL} = 0 \\ &w.r.t.\ \mathbf{D} \end{aligned} \tag{36}$$

In this case one design cycle for this optimization corresponds to one unsteady flow solution and three unsteady adjoint solutions, one adjoint solution for the the objective and one adjoint solution for each constraint. The noise signature of the resulting optimum rotor provides a limit of the achievable noise reduction, but it will come at the expense of the rotor's performance as detailed in the following sections.
Hence, the last optimization is a multidisciplinary aeroacoustic optimization and aims at reducing the noise signature of the Hart2 rotor in trimmed forward flight without suffering any torque penalty according to equation (37).

$$\begin{aligned} &min\ p'_{RMS} \\ &\texttt{subject to} \\ &L_{THRUST} = 0 \\ &L_{LATERAL} = 0 \\ &L_{TORQUE} < L_{TORQUE_{BASE}} \\ &w.r.t.\ \mathbf{D} \end{aligned} \tag{37}$$

In this case one design cycle consists of one unsteady flow solution, and four unsteady adjoint solutions.
The functionals L_{THRUST}, $L_{LATERAL}$ and L_{TORQUE} are defined as

$$\begin{aligned} L_{THRUST} &= \frac{1}{N}\left(\sum_{i=1}^{N}\left(C_T^i - C_{T_{AVERAGE}}^i\right)\right)^2 \\ L_{LATERAL} &= \frac{1}{N}\left[\left(\sum_{i=1}^{N} C_{M_x}^i\right)^2 + \left(\sum_{i=1}^{N} C_{M_y}^i\right)^2\right] \\ L_{TORQUE} &= \frac{1}{N}\sum_{i=1}^{N}\left(C_Q^i\right)^2 \end{aligned} \tag{38}$$

where $C_{T_{AVERAGE}}^i = 0.0044$ is the target thrust coefficient for the baseline Hart2 rotor. The flow conditions are those described in section IV and the simulations are run for two rotor revolutions using a 2 degree timestep and a computational mesh that consists of approximately 2.32 million nodes. The aerodynamic functionals in equation (38) are accumulated only over the second revolution to prevent the optimization algorithm from focusing on the initial

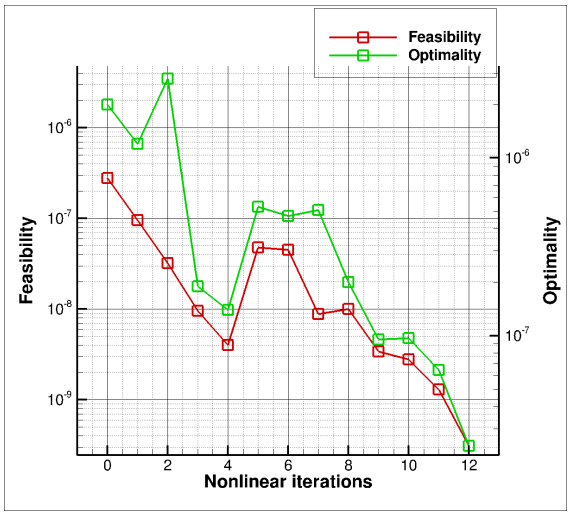

(a) Feasibility and optimality of the trim problem as a function of nonlinear optimization iterations

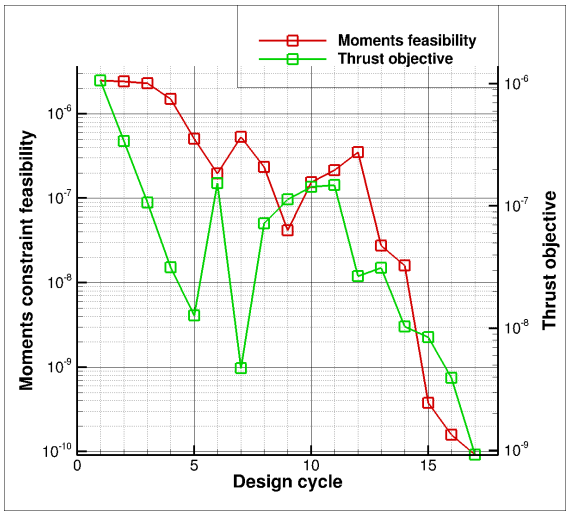

(b) Convergence of the thrust objective function and moment constraint as a function of design cycles.

Figure 4. Convergence of the trim optimization problem

transient. The acoustic integration is performed only over the second revolution and the acoustic objective function is evaluated over the observer time window shown in Figure 2(b). For all optimizations the observer is stationary and is placed in front of the rotor as shown in Figure 1(b) and detailed in Table 1.

The baseline blade is constructed by stacking 9 airfoils along the span. Each airfoil is parameterized with 10 Hick-Henne bump function, 5 for the upper surface and 5 for the lower surface respectively. Blade twist varies linearly between root and tip, while one collective and two cyclics allow the trimming of the rotor, for a total of 95 design variables in the vector of design variables $\mathbf{D}$ in equation (36) and (37).

One unsteady flow solution takes approximately one hour of wall-clock time on 1024 cores with each unsteady adjoint solution costing approximately the same as the flow solution, so that the cost of one design cycle spans from three hours for the trim optimization, equation (35), to five hours for the aeroacoustic optimization, equation (37). The SNOPT[38] sequential quadratic programming algorithm is used to drive the constrained optimization. The computational cost of any of the optimizations in equation (36) or (37) is approximately 96 hours of wall-clock time on 1024 cores on the Yellowstone supercomputer at the NCAR-Wyoming Supercomputing Center (NWSC).

Trim results

The trim optimization problem is described by equation (35). The optimization convergence is shown in Figure 4. After 9 nonlinear iterations and 17 design cycles the feasibility and optimality of the optimization problem are reduced by more than 2 orders of magnitude and the baseline Hart2 rotor is trimmed as further confirmed by thrust and lateral moments time histories shown in Figure 5. The trimmed Hart2 rotor will now serve as the initial design for all subsequent aeroacoustic optimizations.

Aeroacoustic optimization

As mentioned above the initial design is the trimmed Hart2 rotor from the previous section and the optimization problem is described in equation (36). SNOPT convergence is shown in terms of nonlinear optimization iterations and design cycles in Figure 6. After 17 design cycles the optimization produces a geometry that reduces the Overall Sound Pressure Level of 3.4 dB while keeping the rotor trimmed as highlighted by the thrust and lateral moments time histories shown in Figure 7. The acoustic pressure time history is shown in Figure 8. Thickness loading is only slightly affected by the optimization that acts mainly on the loading pressure to minimize the total acoustic pressure. The noise minimization is achieved with rather thick airfoils especially at the inboard sections, as shown in Figure 9. Since rotor torque is not included in the optimization, the noise reduction achieved here, despite representing the maximum noise reduction achievable within the current optimization framework, comes at the expense of rotor performance, as clearly indicated in Figure 10. Consequently the next step is to introduce a torque constraint in the optimization process.

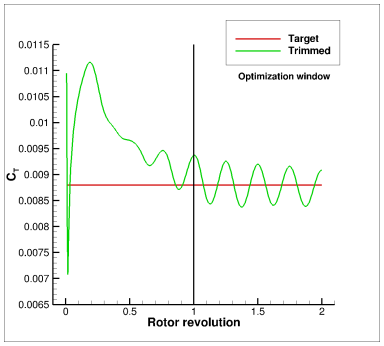

(a) Target and computed thrust time history for the trimmed Hart2 rotor

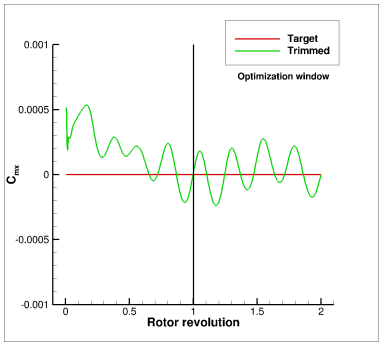

(b) Target and computed roll moment time history for the trimmed Hart2 rotor

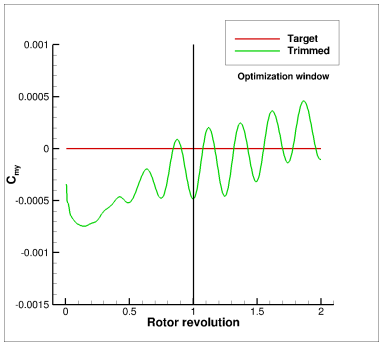

(c) Target and computed pitch moment time history for the trimmed Hart2 rotor

Figure 5. Thrust and moments time histories for the trimmed baseline Hart2 rotor

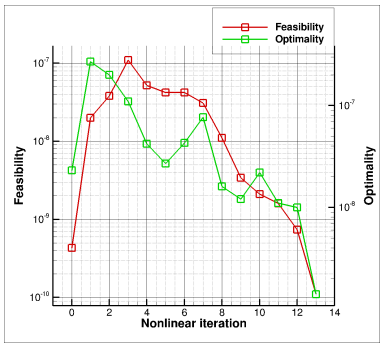

(a) Feasibility and optimality for the aeroacoustic optimization problem as a function of nonlinear iterations

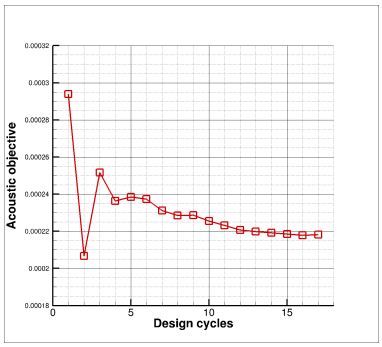

(b) Convergence of the aeroacoustic objective function as a function of design cycles.

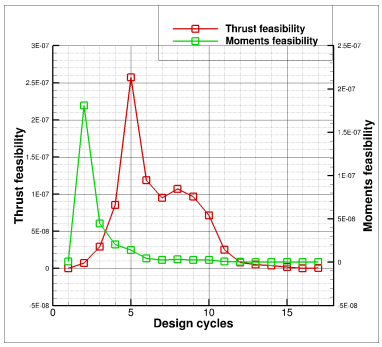

(c) Convergence of the trim constraint as a function of design cycles.

Figure 6. Convergence of the aeroacoustic optimization problem

Torque-constrained aerocoustic optimization

The initial design for this multidisciplinary aeroacoustic optimization is again the trimmed Hart2 rotor and the optimization problem is described in equation (37). After 20 design cycles the acoustic objective function settles down while attaining the same torque level as the baseline Hart-2 rotor, as shown in Figure 11(b), and the trim constraint feasibility, shown in Figure 11(c), is comparable to the baseline geometry, highlighting that the optimized rotor is trimmed, as confirmed by the thrust and lateral moments time histories shown in Figure 12. Contrary to the aeroacoustic optimization, the torque level for the torque-constrained aeroacoustically optimized rotor is the same as that of the baseline Hart2 rotor as shown in Figure 13. The acoustic pressure time history at the observer is shown in Figure 14. The optimized rotor is 1.7 dB quieter in terms of Overall Sound Pressure Level and, again, noise mitigation is achieved by acting mainly on the loading pressure as in the previous optimization. A comparison between the baseline and optimized airfoils is shown in Figure 15 where it can be seen that again the optimized shapes tend to be thicker at the inboard stations and thinner at the outboard ones.

Previous noise mitigation studies[39] have shown that optimizing for one observer location can result in higher noise levels at different observer locations. A directivity study for the optimized rotor reveals that the current design is capable of reducing noise at in-plane observer locations that have not been targeted by the optimization as shown for two different observers placed at $\psi = 135$ and $\psi = 315$ degrees as shown in Figure 16.

VI. Conclusions and Future work

We successfully developed a 3 dimensional adjoint-based formulation for the hybrid approach to the acoustic propagation problem for rotorcraft noise. The new adjoint formulation has been applied to the multidisciplinary problem of the noise minimization for the Hart2 rotor in trimmed forward flight with no torque penalty. Results

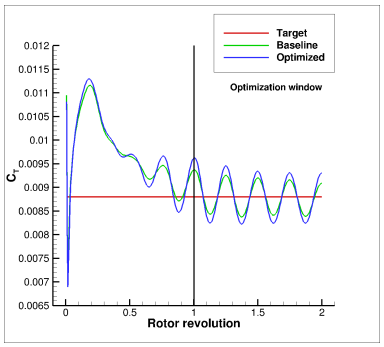

(a) Thrust time history for the baseline and the aeroacoustically optimized trimmed Hart2 rotor

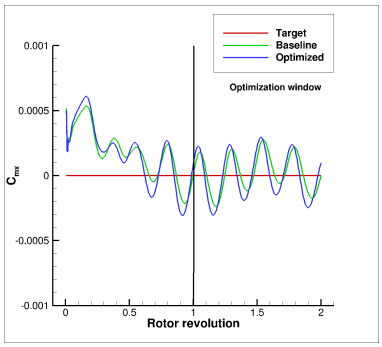

(b) Rolling moment time history for the baseline and the aeroacoustically optimized trimmed Hart2 rotor

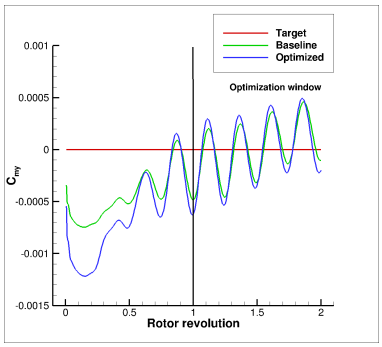

(c) Pitching moment time history for the baseline and the aeroacoustically optimized trimmed Hart2 rotor

Figure 7. Thrust and moment time histories for the aeroacoustically optimized Hart2 rotor

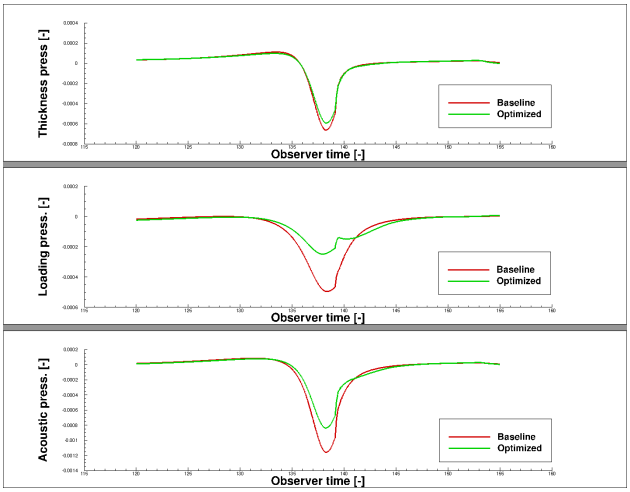

Figure 8. Thickness, loading and total acoustic pressures at the observer for the aeroacoustically optimized rotor

presented here highlight the potential of multidisciplinary design optimization for rotorcraft design problem. Future work will focus on extending the current multidiscplinary design capability by including blade flexibility effects in the aeroacoustic optimization. Additional design variables to account for planform shape changes will be considered. Different acoustic problems, e.g. a windtunnel formulation, will also be investigated.

VII. Acknowledgements

This work was partly funded by the Alfred Gessow Rotorcraft Center of Excellence through a subcontract with the University of Maryland. Computer resources were provided by the University of Wyoming Advanced Research Computing Center and by the NCAR-Wyoming Supercomputer Center. We would like to thank Dr. Brentner for making PSU-WOPWOP available to us for validation purposes.

References

[1]Jameson, A. and Vassberg, J., "Computational Fluid Dynamics for Aerodynamic Design: Its Current and Future Impact," *Proceedings of the 39th Aerospace Sciences Meeting and Exhibit, Reno NV*, 2001, AIAA Paper 2001–0538.

[2]Lyu, Z., Kenway, K. W., and Martins, J. R. R. A., "Aerodynamic Shape Optimization Investigation of the Common Research Model Wing Benchmark," *AIAA Journal*, Vol. 53-4, 2015, pp. 968–985.

[3]Nielsen, E. and Anderson, W., "Recent Improvements in Aerodynamic Design Optimization on Unstructured Meshes," *AIAA Journal*, Vol. 40, No. 6, June 2002, pp. 1155–1163.

[4]Jameson, A. and Martinelli, L., "Aerodynamic shape optimization techniques based on control theory," *Computational Mathematics Driven*

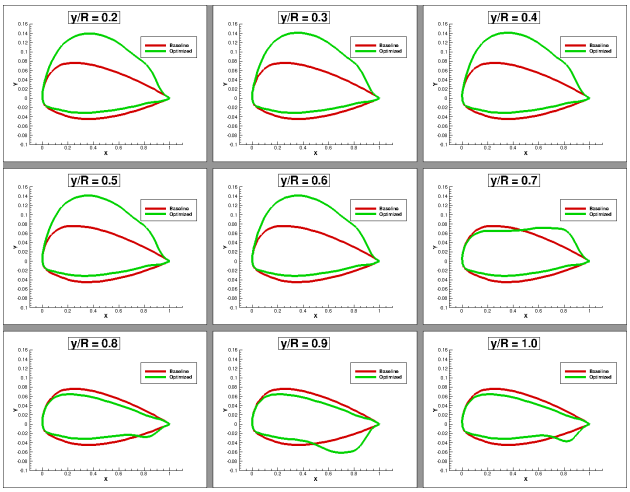

Figure 9. Baseline and optimized airfoil shapes for the aeroacoustically optimized rotor

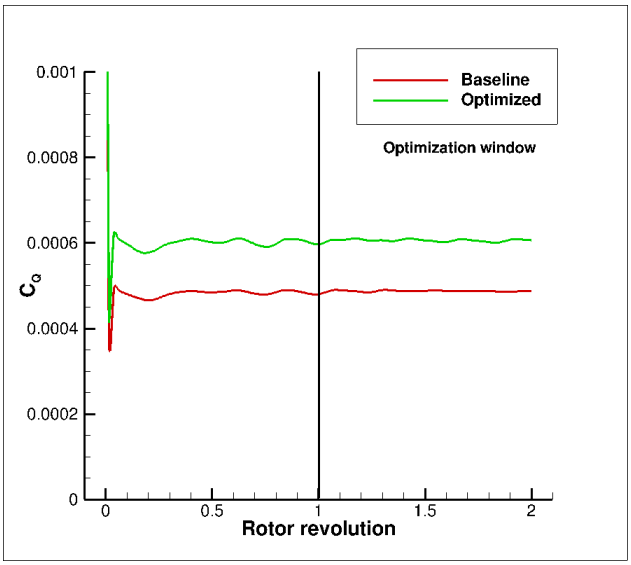

Figure 10. Baseline and optimized torque time histories for the aeroacoustically optimized rotor showing the performance penalty paid to minimize the acoustic signature.

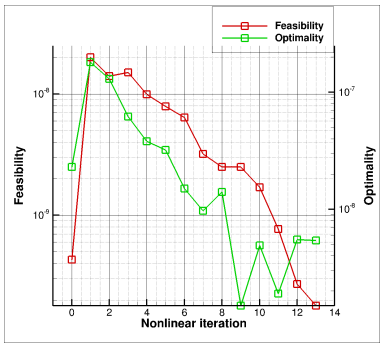

(a) Feasibility and optimality for the torque-constrained aeroacoustic optimization problem as a function of nonlinear iterations

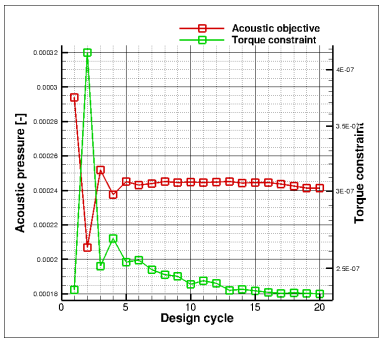

(b) Convergence of the acoustic objective function and the torque constraint as a function of design cycles.

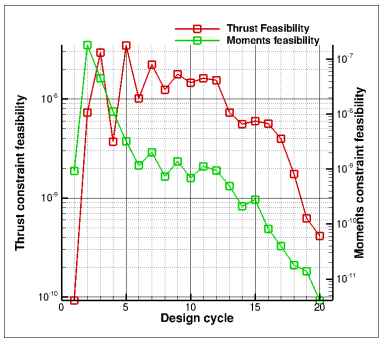

(c) Convergence of the trim feasibility as a function of design cycles.

Figure 11. Convergence of the torque-constrained aeroacoustic optimization problem

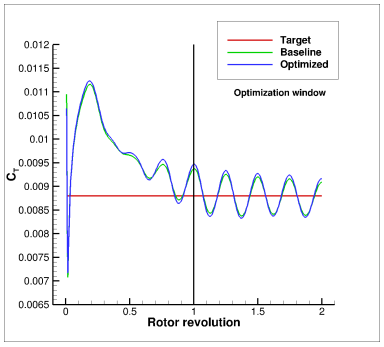

(a) Thrust time history for the baseline and torque-constrained aeroacoustically optimized trimmed Hart2 rotor

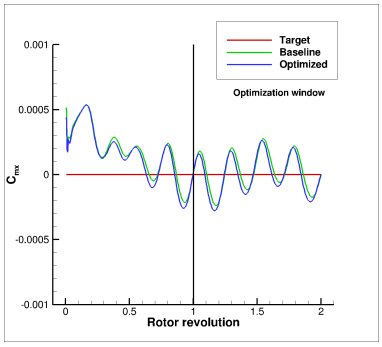

(b) Rolling moment time history for the baseline and the torque-constrained aeroacoustically optimized trimmed Hart2 rotor

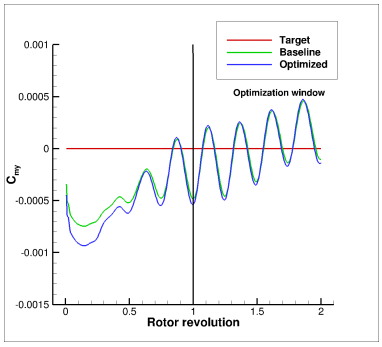

(c) Pitching moment time history for the baseline and the torque-constrained aeroacoustically optimized trimmed Hart2 rotor

Figure 12. Thrust and moment time histories for baseline and the torque-constrained aeroacoustically optimized trimmed Hart2 rotor

by Industrial Problems, edited by R. Burkard, A. Jameson, G. Strang, P. Deuflhard, J.-L. Lions, V. Capasso, J. Periaux, and H. Engl, Vol. 1739 of *Lecture Notes in Mathematics*, Springer Berlin Heidelberg, 2000, pp. 151–221.

[5]Kim, S., J., A., and Jameson, A., "Multi-Element High-Lift Configuration Design Optimization Using Viscous Continuous Adjoint Method," *Journal of Aircraft*, Vol. 41, No. 5, 2004, pp. 1082–1097.

[6]K., N. S., Jameson, A., and Alonso, J., "Adjoint-Based Sonic Boom Reduction for Wing-Body Configurations in Supersonic Flow," *Canadian Aeronautics and Space Journal*, Vol. 51, No. 4, 2005.

[7]Bisson, F. and Nadarajah, S., "Adjoint-Based Aerodynamic Optimization of Benchmark Problems," *53rd AIAA Aerospace Sciences Meeting, Kissimmee, Fl*, January 2015, AIAA Paper 2015-1948.

[8]Lee, C., Telidetzki, K., Buckley, H., Gagnon, H., and Zingg, D. W., "Aerodynamic Shape Optimization of Benchmark Problems Using Jetstream," *53rd AIAA Aerospace Sciences Meeting, Kissimmee, Fl*, January 2015, AIAA Paper 2015-0262.

[9]Giles, M., Duta, M., Muller, J., and Pierce, N. A., "Algorithm Developments for Discrete Adjoint Methods," *AIAA Journal*, Vol. 41, No. 2, February 2003, pp. 198–205.

[10]Mavriplis, D. J., "Solution of the Unsteady Discrete Adjoint for Three-Dimensional Problems on Dynamically Deforming Unstructured Meshes," *Proceedings of the 46th Aerospace Sciences Meeting and Exhibit, Reno NV*, 2008, AIAA Paper 2008–0727.

[11]Nielsen, E. and Diskin, B., "Discrete Adjoint-Based Design for Unsteady Turbulent Flows on Dynamic Overset Unstructured Grids," *50th AIAA Aerospace Sciences Meeting and Exhibit, Nashville, TN*, January 9-12 2012, AIAA Paper 2012–0554.

[12]Kenway, G. K. W., Kennedy, G. J., and Martins, J. R. R. A., "Scalable parallel approach for high-fidelity steady-state aeroelastic analysis and adjoint derivative computations," *AIAA Journal*, 2013, (In press).

[13]Mishra, A., Mani, K., Mavriplis, D. J., and Sitaraman, J., "Helicopter Rotor Design using Adjoint-based Optimization in a Coupled CFD-CSD Framework," *69th American Helicopter Society Annual Forum, Phoenix, AZ*, May 21–23 2013.

[14]Edwards, B. and Cox, C., "Revolutionary concepts for Helicopter Noise Reduction - S.I.L.E.N.T Program," Tech. Rep. CR-2002-211650, NASA, May 2002.

[15]Yu, Y. H., "Rotor blade vortex interaction noise," *Progress in Aerospace Sciences*, Vol. 36, 2000, pp. 97–115.

[16]Rumpfkeil, M. and Zingg, D., "A General Framework for the Optimal Control of Unsteady Flows with Applications," *45th AIAA Aerospace Sciences Meeting and Exhibit, Reno, NV, January*, 2007, AIAA Paper 2007–1128.

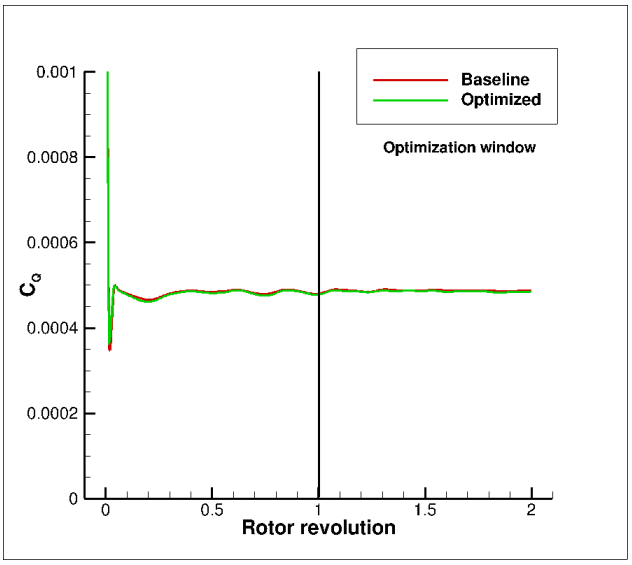

Figure 13. Baseline and optimized torque time histories for the torque-constrained aeroacoustically optimized rotor.

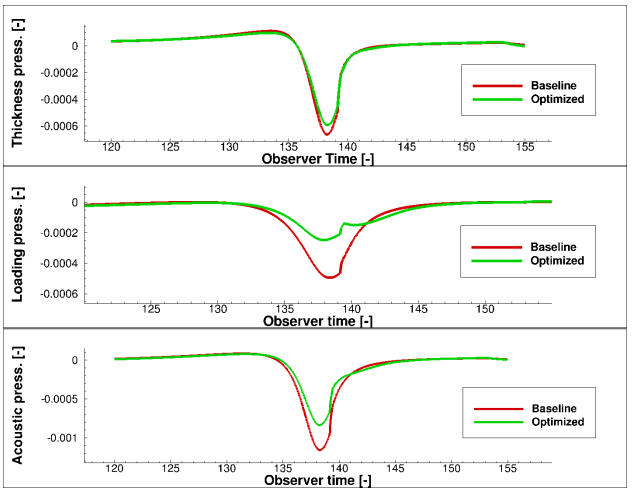

Figure 14. Thickness, loading and total acoustic pressures at the observer

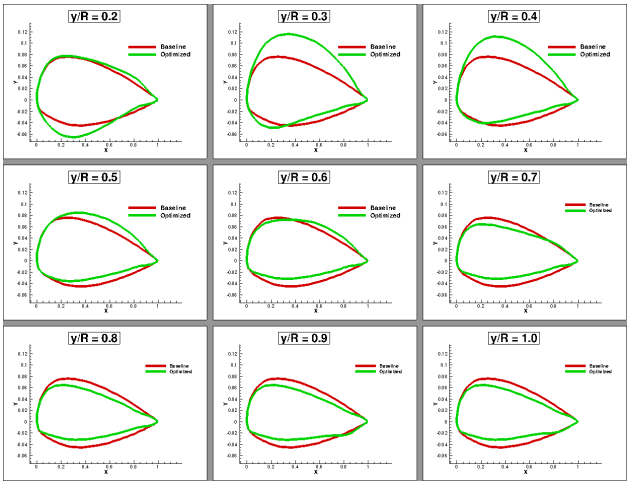

Figure 15. Torque-constrained aeroacoustically optimized airfoil shapes

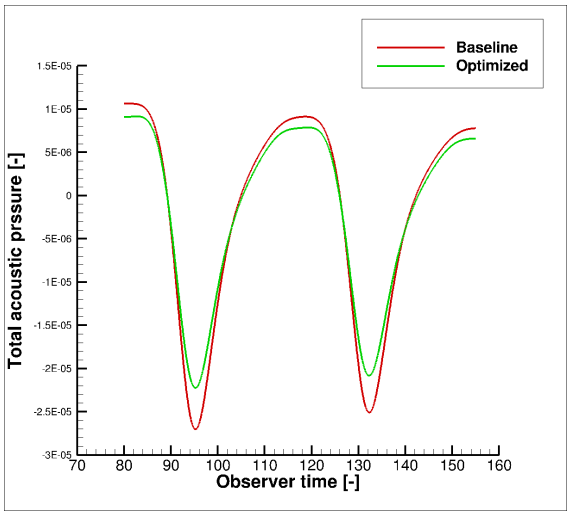

(a) Baseline and optimized total acoustic time history at $\psi = 135$ degrees

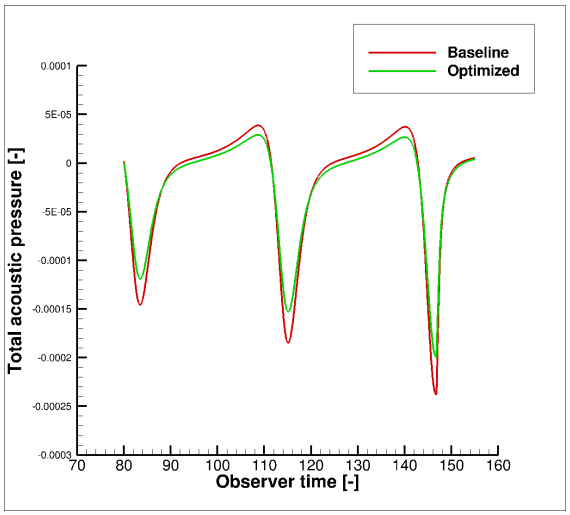

(b) Baseline and optimized total acoustic time history at $\psi = 315$ degrees

Figure 16. Directivity study for the baseline and optimized geometry

[17]Economon, T. D., Palacios, F., and Alonso, J. J., "A Coupled-Adjoint Method for Aerodynamic and Aeroacoustic Optimization," *14th AIAA/ISSM Multidisciplinary Analysis and Optimization Conference*, 2012, AIAA Paper 2012–5598.

[18]Rallabhandi, S. K., Nielsen, E. J., and Diskin, B., "Sonic Boom Mitigation Through Aircraft Design and Adjoint Methodology," *30th AIAA Applied Aerodynamics Conference*, 2012, AIAA Paper 2012–3220.

[19]Fabiano, E., Mavriplis, D. J., and Sitaraman, J., "Adjoint - based Aeroacoustic Design Optimization for Blade Vortex Interaction Noise," *53rd AIAA Aerospace Sciences Meeting*, January 4–8 2015, AIAA Paper 2015–1801.

[20]Mavriplis, D. J., "Discrete Adjoint-Based Approach for Optimization Problems on Three-Dimensional Unstructured Meshes," *AIAA Journal*, Vol. 45-4, April 2007, pp. 741–750.

[21]Mani, K. and Mavriplis, D. J., "Geometry Optimization in Three-Dimensional Unsteady Flow Problems using the Discrete Adjoint," *51st AIAA Aerospace Sciences Meeting, Grapevine, TX*, January 2013, AIAA Paper 2013-0662.

[22]Mishra, A., Mani, K., Mavriplis, D. J., and Sitaraman, J., "Time-dependent Adjoint-based Optimization for Coupled Aeroelastic Problems," *21st AIAA CFD Conference, San Diego, CA*, June 24–27 2013, AIAA Paper 2013–2906.

[23]Spalart, P. R. and Allmaras, S. R., "A One-equation Turbulence Model for Aerodynamic Flows," *La Recherche Aérospatiale*, Vol. 1, 1994, pp. 5–21.

[24]Mavriplis, D. J., "Multigrid Strategies for Viscous Flow Solvers on Anisotropic Unstructured Meshes," *Journal of Computational Physics*, Vol. 145, No. 1, Sept. 1998, pp. 141–165.

[25]Yang, Z. and Mavriplis, D. J., "A Mesh Deformation Strategy Optimized by the Adjoint Method on Unstructured Meshes," *AIAA Journal*, Vol. 45, No. 12, 2007, pp. 2885–2896.

[26]Mavriplis, D. J., Yang, Z., and Long, M., "Results using NSU3D for the first Aeroelastic Prediction Workshop," *Proceedings of the 51st Aerospace Sciences Meeting and Exhibit, Grapevine TX*, 2013, AIAA Paper 2013–0786.

[27]Mavriplis, D. J., "Time Dependent Adjoint Methods for Single and Multi-disciplinary Problems," *38th VKI Lecture Series on Advanced Computational Fluid Dynamics. Adjoint methods and their application in Computational Fluid Dynamics. von Karman Institute of Fluid Dynamics, Rhode St Genese, Belgium*, 2015.

[28]Mani, K. and Mavriplis, D. J., "Adjoint based sensitivity formulation for fully coupled unsteady aeroelasticity problems," *AIAA Journal*, Vol. 47, No. 8, Aug. 2009, pp. 1902–1915.

[29]Mishra, A., , Mavriplis, D. J., and Sitaraman, J., "Time-dependent Aero-elastic Adjoint-based Aerodynamic Shape Optimization of Helicopter Rotors in Forward Flight," *53rd AIAA Aerospace Sciences Meeting*, January 4–8 2015, AIAA Paper 2015–1130.

[30]Brentner, K. S. and Farassat, F., "Modeling aerodynamically generated sound of helicopter rotors," *Progress in aerospace sciences*, Vol. 39, 2003, pp. 83–120.

[31]Crighton, D. G., Dowling, A. P., and Ffowcs Willliams, J. E., *Modern Methods in Analytical Acoustics*, Springer-Verlag, 1992.

[32]Brentner, K. S. and Farassat, F., "An Analytical Comparison of The Acoustic Analogy And Kirchoff Formulation For Moving Surfaces," *AIAA Journal*, Vol. 36-8, 1998, pp. 1379–1386.

[33]Yu, Y. H., Tung, C., van der Wall, B., Pausder, H.-J., Burley, C., Brooks, T., Beaumier, P., Delrieux, Y., Mercker, E., and Pengel, K., "The HART-II Test: Rotor Wakes and Aeroacoustics with Higher-Harmonic Pitch Control (HHC) Inputs -The Joint German/French/Dutch/US Project-," *58th American Helicopter Society Annual Forum, Montreal, Canada*, June 11–13 2002.

[34]Farassat, F. and Succi, G. P., "The prediction of helicopter discrete frequency noise," *Vertica*, Vol. 7-4, 1983, pp. 309–320.

[35]di Francescantonio, P., "A New Boundary Integral Formulation for the Prediction of Sound Radiation," *Vertica*, Vol. 7-4, 1983, pp. 309–320.

[36]Bres, G. A., Brentner, K. S., Perez, G., and Jones, H. E., "Maneuvering rotorcraft noise prediciton," *Journal of sound and vibration*, Vol. 275, 2004, pp. 719–738.

[37]Martins, J. R. R. A. S. P. and Alonso, J. J., "The Complex-Step Derivative Approximation," *ACM Transactions on Mathematical Software*, Vol. 29-3, 2003, pp. 245–262.

[38]Gill, P. E., Murray, W., and Saunders, M. A., "SNOPT: An SQP Algorithm for Large-Scale Constrained Optimization," *SIAM review*, Vol. 47-1, 2005, pp. 99–131.

[39]Sim, B. W., JanakiRam, R. D., Barbely, N. L., and Solis, E., "Reduced In-Plane, Lowe Frequency Noise of an Active Flap Rotor," *American Helicopter Society 65th Annual Forum*, Grapevine, TX, May 2009.